Heliyon 9 (2023) e20822

Contents lists available at ScienceDirect

Heliyon

journal homepage: www.cell.com/heliyon

Fabrication and characterization of novel, cost-effective graphitic carbon nitride/Fe coated textile nanocomposites for effective degradation of dyes and biohazards

Munir Ashraf [a,1], Fiaz Hussain [b,1], Humera Aziz [c,d,*], Umair Riaz [e], Muhammad Hamzah Saleem [f], Amjed Javid [a], Anum Nosheen [a], Azam Ali [g], Mohammad K. Okla [h], Ibrahim A. Saleh [i], Ibrahim A. Alaraidh [h], Mostafa A. Abdel-Maksoud [h]

[a] *Functional Textiles Research Group, School of Engineering & Technology, National Textile University, Faisalabad, 37610, Pakistan*
[b] *Department of Fibre and Textile Technology, University of Agriculture, Faisalabad, Pakistan*
[c] *Department of Agricultural Sciences, College of Agriculture and Environmental Sciences, Government College University, Faisalabad, 38040, Pakistan*
[d] *Department of Environmental Sciences, College of Agriculture and Environmental Sciences, Government College University, Faisalabad, 38040, Pakistan*
[e] *Department of Soil and Environmental Sciences, MNS-University of Agriculture, Multan, 60000, Pakistan*
[f] *College of Plant Science and Technology, Huazhong Agricultural University, Wuhan, 430070, China*
[g] *Department of Material Engineering, Technical University of Liberec, Liberec, Czech Republic*
[h] *Botany and Microbiology Department, College of Science, King Saud University, P.O. Box 2455, Riyadh, 11451, Saudi Arabia*
[i] *Faculty of Science, Zarqa University, Zarqa, 13110, Jordan*

ARTICLE INFO

Keywords:
Nanocomposite
Photocatalyst
Antibacterial
Antiviral
Recyclability
Graphitic carbon nitride

ABSTRACT

Textile-based photocatalysts are the new materials that can be utilized as an effective sustainable solution for biochemical hazards. Hence, we aimed to develop a sustainable, cost-effective, and facile approach for the fabrication of photocatalytic fabric using graphitic carbon nitride (g-C_3N_4) and ferric-based multifunctional nanocomposite. Bulk g-C_3N_4 was prepared from urea by heating it at 500 °C for 2 h. The structure of ball-milled g-C_3N_4 was engineered by doping with various amounts of iron (III) chloride hexahydrate solution (0.006 mol/L) and sintered at 90 °C for 24 h to prepare g-C_3N_4–nanosheets/α-Fe_2O_3 composites. These nanocomposites have potential avenues towards rational designing of g-C_3N_4 for improved photocatalytic, antibacterial, and antiviral behavior. The prepared nanocomposite was characterized for its surface morphology, chemical composition, crystal structure, catalytic, antibacterial, and antiviral behavior. The fabrication of ferric doped g-C_3N_4 nanocomposites was characterized by SEM, EDX, FTIR, and XRD analysis. The coated fabric nanocomposite was characterized for methylene blue dye degradation under visible light, antibacterial and antiviral behavior. The developed textile-based photocatalyst has been found with very good recyclability with photocatalytic degradation of dye up to 99.9 % when compared to conventional g-C_3N_4 powder-based photocatalyst.

* Corresponding author. Department of Agricultural Sciences, College of Agriculture and Environmental Sciences, Government College University, Faisalabad, 38040, Pakistan.
E-mail address: humeraaziz.uaf@gmail.com (H. Aziz).
[1] Both authors contributed equally as the first author.

https://doi.org/10.1016/j.heliyon.2023.e20822
Received 8 May 2023; Received in revised form 28 September 2023; Accepted 8 October 2023
Available online 13 October 2023

1. Introduction

Biochemical hazards refer to substances or agents that can cause harm to living organisms or the environment [1]. Biochemical hazards include microorganisms such as bacteria, viruses, fungi, and parasites that can cause infectious disease as well as substances that can cause harm to human health or the environment due to their toxic, corrosive, or flammable properties [2]. These hazards arise from exposure to industrial chemicals, pesticides, heavy metals, and other hazardous materials [3,4]. The textile industry is one of the major sources of hazardous substances in the form of solvents, dyes, and other materials and microorganisms in the processing of textiles [5]. The development of functional textiles with antibacterial and antiviral properties, as well as the treatment of wastewater by the textile industries to remove harmful chemicals and pollutants, can help to mitigate these hazardous components and ensure a safer and more sustainable textile industry [6].

Currently, various types of disinfecting agents and catalysts have been studied to address the great challenges concerned with biochemical hazards. Photocatalytic technologies have the potential to trigger a number of significant chemical reactions (CO_2 reduction, photodecomposition of hydrogen, and degradation of pollutants) by sunlight where it generates disinfecting and catalytic agents to perform the cleaning tasks [7,8]. Several groups of researchers have been trying to introduce the new structure of photo-catalysts such as complexes of metal with metal oxides, metal oxides with carbonaceous metal oxides [9], nanocomposites of Ag/TiO_2 [10], $SnO_2/ZnO/TiO_2$ [11], Ag/SnO_2, etc. [12]. However, some of them are not suitable due to high manufacturing costs, low antibacterial efficiency, and inadequate chemical resistance. Also, they are not suitable for removing contaminants at extremely low concentrations (in the range of parts per billion). Therefore, the development of innovative recyclable multifunctional nanocomposites using sustainable and cost-effective synthesis techniques has gained considerable attention from the research community in both academia and industry [13,14].

Graphitic carbon nitride (g-C_3N_4) has found a strong position among other high-performance photocatalysts because it is developed from urea or melamine which are cheap and abundantly available chemicals in the commercial market [15]. The unique characteristics of g-C_3N_4 such as low toxicity, antibacterial behavior, water splitting, chemical pollutant degradation, good response to visible light, biocompatible in the dark, good resistance against chemical and anti-corrosion make it an ideal candidate for futuristic multifunctional photocatalysts [16–18]. However, low absorption of visible light, high charge recombination rate, and small surface area of the g-C_3N_4 limit its antimicrobial and photocatalytic properties [19]. Furthermore, it is very difficult to recover the g-C_3N_4 catalyst from the solvent even by centrifugation at 14000 rpm, which makes it unsuitable to use after recycling. Various techniques have been adopted such as modification in chemical compositions, varying synthesis temperature, composite structures with semiconductors, and doping with metal particles to enhance the performance properties and characteristics of g-C_3N_4 [20,21].

One promising approach is the development of graphitic carbon nitride (g-C_3N_4)/Fe-coated textiles, which can serve as an effective solution to address the problems of biochemical hazards. Therefore, in this study, we have developed g-C_3N_4/Fe-coated textiles with excellent photocatalytic, antibacterial. To the best of our knowledge, there is no study reported on the doping of g-C_3N_4 with different concentrations of ferric salt and textile-based free-standing recyclable photocatalysts. Moreover, the developed photocatalyst can have excellent reusability thus outperforming the conventional photocatalyst which has the problem of poor recovery. In addition, the developed photocatalyst is highly effective at very low concentration which also makes it superior to conventional photocatalyst. Our developed method is very short, facile, economical, and eco-friendly. At first, the bulk g-C_3N_4 powder was prepared by simple calcination using the ordinary furnace and grinded. Subsequently, the developed Fe-doped g-C_3N_4 nanocomposites were applied to the cotton fabric using the knife-over roller technique. The prepared photocatalysts are firmly coated over the textile structures and do not have problems of leaching, wasting, and recovering from the solvents.

2. Materials and methods

2.1. Materials

Urea (CH_4N_2O) and iron (III) chloride hexahydrate ($FeCl_3{\cdot}6H_2O$) were purchased from Daejung Chemicals (Korea). Methylene blue (MB) was purchased from Sigma Aldrich. Water-born polyurethane solution (Lurapret, NDP.S), thickening agent (Lutexil HIT), and wetting agent (Felosan RGN) were purchased from BASF. The 100 % cotton fabric with GSM (gram per square meter) of 130 was obtained from Sapphire Textiles (Pakistan). All the chemicals used in this study were of reagent grade and used without any further purification.

2.2. Preparation of bulk g-C_3N_4, g-C_3N_4–nanosheets and g–C_3N_4–Fe_2O_3 nanocomposites

The bulk g-C_3N_4 was synthesized by placing urea (20 g) in a ceramic crucible covered with a lid. The ceramic crucible was placed in a heated furnace and the temperature of 500 °C was achieved at a rate of 5 °C/min. The adjusted temperature (500 °C) was given for 2 h. The placed urea was converted into yellow compacted sediments of g-C_3N_4. The obtained yellow compacted g-C_3N_4 was cooled down to room temperature. The powder of g-C_3N_4 was placed into a desiccator to preserve it from moisture uptake.

The second step was the conversion of bulk graphitic carbon nitride g-C_3N_4 into the nanosheets. The as-synthesized g-C_3N_4 was grinded with the help of agate/mortar and converted into fine powder. Subsequently, the powder was subjected to the process of dry pulverized ball milling. For 1 h of dry milling, a sintered corundum vessel with a capacity of 80 ml and zirconium balls with a diameter of 10 mm was utilized. The ball-to-material ratio (BMR) was maintained at 8:1 and the material was grinded at 600 RPM. Hence the

grinded powder was converted into fine nanosheets of g-C_3N_4.

In order to prepare the g-C_3N_4–nanosheets/α-Fe_2O_3 composites, the different concentrations of iron (III) chloride hexahydrate $FeCl_3{\cdot}6H_2O$ salt were selected. The $FeCl_3{\cdot}6H_2O$ aqueous solutions with a concentration of 0.006 mol/L (0, 1 ml, 2 ml, 3 ml, and 4 ml) were mixed with 0.1 g of g–C_3N_4–nanosheets powder. The resulting solutions having different concentrations of $FeCl_3$ were vigorously stirred with the help of a magnetic stirrer at a constant speed of 500 RPM for 30 min. Afterward, the solution was well dispersed by the process of ultra-sonication for 10 min followed by drying at 90 °C in an oven for 12 h. Subsequently, they were annealed for half an hour in the air at 450 °C for the conversion of Fe precursor to crystalline α-Fe_2O_3. The resulting samples were coded as the g–C_3N_4–Fe composites. Hence, we produced a total of 5 samples of g–C_3N_4–Fe nanocomposites against five (0, 1 ml, 2 ml, 3 ml, 4 ml) concentrations of $FeCl_3{\cdot}6H_2O$ salt (0.006 mol/L). The listed samples are shown in Table S1 (SI file).

2.3. Preparation of coating paste by using g-C_3N_4/α-Fe_2O_3 nanosheets

A homogeneous mixture of the water-borne polyurethane, thickening agent, wetting agent, and prepared g–C_3N_4–α-Fe_2O_3 nanocomposites was prepared. For this, 0.50 g of g–C_3N_4–nanosheets/α-Fe_2O_3 composite, thickening agent (0.4 %), and wetting agent (4.0%) were dispersed in 50 ml of polyurethane solution. The resultant solution was mechanically stirred for 2 h at 800–900 rpm. The thickening agent is used to maintain rheological properties and uniform application of paste while the wetting agent is utilized to create micro porosity. The prepared homogeneous paste was placed into a vacuum oven for 24 h to eliminate the bubbles.

2.4. Coating of g–C_3N_4–nanosheets/α-Fe_2O_3 on fabric

Prior to coating, the mercerized cotton fabric (3×10 inch^2) was made alkaline by immersing the fabric in 10% sodium hydroxide (NaOH) solution. Following this, the fabric was squeezed between the padder rollers at a pressure of 1.5 bar and dried in a stenter at 120 °C for 10 min. Afterward, the as-prepared g–C_3N_4–nanosheets/α-Fe_2O_3 paste was applied to the fabric through the knife over-roller method. The coated fabric was passed through a padder to expel the excess amount of coating from the fabric followed by drying in a stenter at 120 °C for 1 min and curing at 150 °C for 3 min. The fabric was coated three-fold to ensure that the g–C_3N_4–nanosheets/α-Fe_2O_3 composite is uniformly applied to the fabric. The average coating thickness achieved was about 0.02 mm. The coated fabric was then subsequently washed with distilled water for 1 h at 40 °C in a low-pressure jigger machine, squeezed, and dried at 100 °C. The design of the experiment for the preparation of all coated fabrics is shown in Table 1.

2.5. Characterization

Fourier transform infrared spectroscopy (FTIR) investigation (Nexus-870) was done to analyze the surface functional groups of as-synthesized composites. The X-ray diffractometer (XRD, Bruker D8 Advance) with Cu Kα radiation ($\lambda = 0.154178$ nm) was used to determine the phases of the as-synthesized composites. SEM (TESCAN, Dortmund-Germany) has been used to examine the surface morphology of coated fabrics by supplying an accelerating voltage using the Tescan VEGA III SEM instrument. The element percentages by weight were measured through EDX characterization. A UV-2700 spectrophotometer (Shimadzu) was used to investigate diffuse reflectance spectra (DRS). An F-4600 FL spectrophotometer was used to acquire the photoluminescence (PL) spectrum.

2.6. Photocatalytic activity

Photocatalytic activity of all composites of g-C_3N_4–nanosheets/α-Fe_2O_3 was determined by the following method, developed by Fiaz et al. with a little modification [22]. The photocatalytic activity of the developed nanocomposites was examined by

Table 1
Design of experiments for the coated fabric samples.

Sr #	Name of fabric sample	Sample name of coating paste	**Code of nanocomposites**	Number of applied coatings	Rate constant K_{app} (min^{-1})
1	F1	P1	GF0	1	0.03
2	F2			2	0.17
3	F3			3	0.26
4	F4	P2	GF1	1	0.05
5	F5			2	0.21
6	F6			3	0.29
7	F7	P3	GF2	1	0.31
8	F8			2	0.43
9	F9			3	0.78
10	F10	P4	GF3	1	0.30
11	F11			2	0.42
12	F12			3	0.79
13	F13	P5	GF4	1	.0.28
14	F15			2	0.40
15	F16			3	0.75

photodegradation of methylene blue (MB) in an aqueous solution at room temperature. Two solar simulators (MASTER TL-D 90 De Luxe 36W/965 SLV/10) were used to provide visible light irradiation for the photocatalytic degradation of MB. Before irradiation, a fabric sample of square shape (1.5 × 1.5 inch^2) containing 0.14 mg of the developed photocatalyst and 40 ml of freshly prepared solution of MB (1 × 10^{-3}) were stirred continuously at 250 rpm for 30 min in a glass reactor to attain the equilibrium adsorption/-desorption between textile substrate-based photocatalyst and MB. For each pre-determined irradiation time, about 2 ml of the reacted solution was withdrawn. A UV–Vis–NIR spectrophotometer (UV-3600, Shimadzu) was used to estimate the residual concentration of MB at 664 m (λ_{max} of MB).

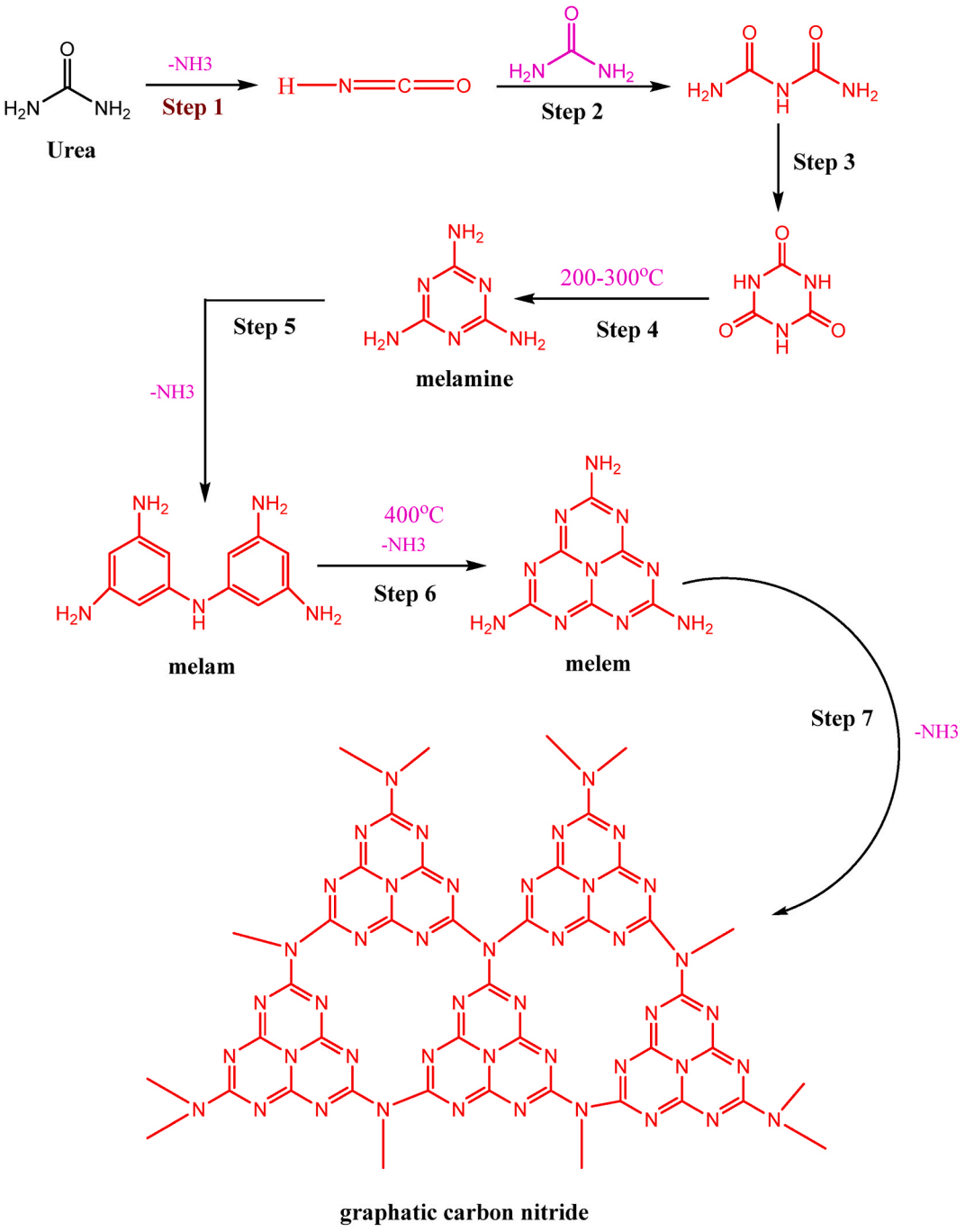

Fig. 1. Reaction scheme for graphitic carbon nitride (g-C_3N_4) formation from urea precursor.

3. Results and discussion

3.1. Reaction mechanism for the synthesis of graphitic carbon nitride, and attachment to the fabric structure

The reaction scheme for graphitic carbon nitride (g-C_3N_4) formation using urea precursor is given in Fig. 1. The urea precursor undergoes a sequence of pyrolysis-generated condensation reactions related to the release of ammonia gas for melamine formation (Step 1–4) which undergoes a nucleophilic addition reaction to form melam (Step 5). Upon further raising the temperature to 400 °C, melam is converted to melem (Step 6), which then polymerizes into the final g-C_3N_4 product with subsequent elimination of ammonia gas (Step 7). The possible structure of iron-doped graphitic carbon nitride is shown in Fig. S1 (Supplementary Information: SI file).

The prepared nanocomposites were deposited on the surface of pure cotton fabric. As cotton fibers are composed of cellulosic structures. Due to the enrichment of anionic sites, free hydroxyl and carboxylic acid groups present on the substrate, the fibers were able to make possible ionic attraction and hydrogen bonds. Furthermore, due to the heterogenic nature of cotton cellulose and voids present in fiber and textile structure, further uptake of nanocomposites was supported.

3.2. Photocatalytic reduction of organic pollutant

Photocatalytic behavior of the developed nanocomposites doped with different concentrations of ferric was determined by the photodegradation of MB (1 mM, initial concentration) under visible light (350-W xenon light). The ultraviolet light (400 nm) was filtered out during the photodegradation process. It is important to note that without the addition of developed photocatalysts the characteristic peak of MB at 664 nm (λ_{max}) does not disappear even after 48 h.

It is obvious from Fig. 2, that under the same conditions of the reaction mixture, the addition of developed nanocomposites results in a decreased intensity of the characteristics peak of MB. The gradual reduction in the peak of MB at 664 nm (λ_{max}) continues until it disappeared, which indicated that MB has significantly reduced to LMB, with a clear change of color from blue to transparent (Fig. 4f). Depending upon the catalytic efficiency of the various nanocomposites, the photocatalytic reduction process is completed at different intervals of time (Fig. 2).

The effect of the developed photocatalysts (P1–P5) dose on the reaction kinetics was evaluated by applying the various content of catalysts by coating process (1–3 coating cycle). The results for the reduction of MB using different photocatalysts (P1–P5) are summarized in Table S2 (SI file).

It is obvious from the results that the rate of MB reduction has increased with the increasing amount of developed photocatalysts. Furthermore, doped nanocomposites have significantly higher catalytic rate in comparison to pure g-C_3N_4 samples. Initially, the doping of g-C_3N_4 resulted in an increased catalytic rate until it reached an optimum level (P3, GF2). Further, an increase in ferric doping resulted in decreased reduction rate of MB. For clarity and ease of understanding, the real-time degradation of MB in the presence of our best sample (P3; F7, F8, F9) was monitored using UV–vis spectrograms and compared with samples F3 (Fig. 2a–e). The photocatalytic degradation process of the MB was fitted to pseudo-first-order kinetics and the reaction rate constant k_{app} can be

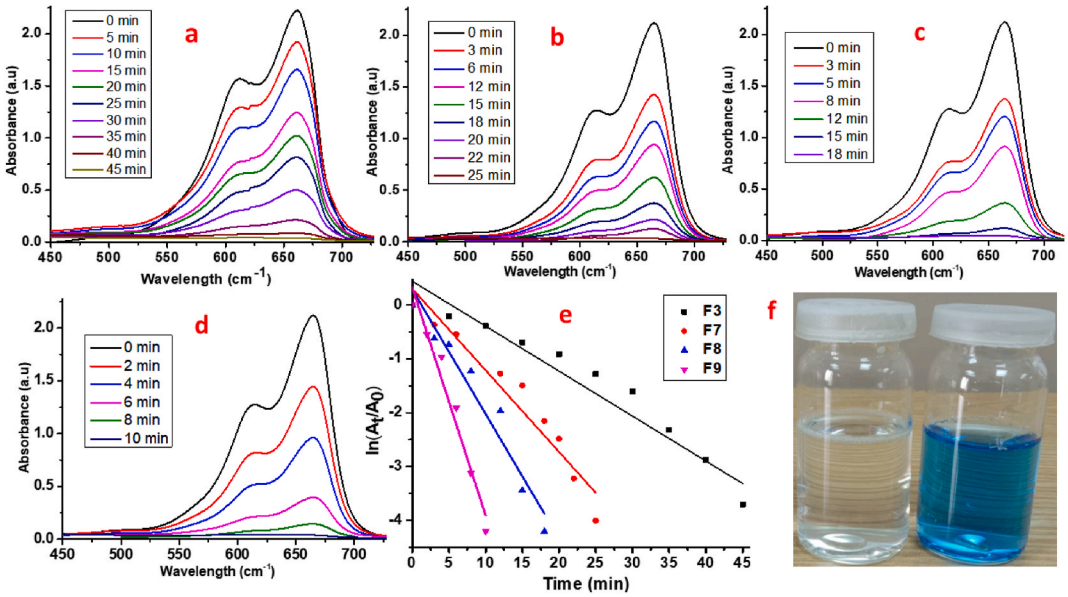

Fig. 2. UV–vis absorption spectra **(a–d)** for the photodegradation of MB in the presence of developed fabricated photocatalysts; Sample F3 **(a)** Sample F7 **(b)** Sample F8 **(c)** Sample F9 **(d)**, Plot of ln(A_t/A_o) versus time for reduction of MB dye to LMB **(e)**, and optical image of MB (right) and reduced LMB (left) **(f)**.

determined as the corresponding slope of the fitting line and the corresponding results are given in Fig. 2e. Fig. 2f shows that the dye solution is completely clear after degradation.

The degradation rates of Sample P1 containing pure g-C_3N_4 nanocatalyst are lower compared to other samples. It can be attributed to the recombination of photogenerated electron-hole pairs throughout the monomeric carbon nitride which restricts quantum efficiency improvement. It is important to note that in the presence of fabric samples (F3 and F9) and irradiation of visible light, the MB degrades almost completely (99.8 %) with a reaction rate constant (K_{app}) of 0.16 and 0.78, respectively. We found that the F9 sample has 4.9 times higher catalytic rate compared to the F3 sample, containing pure g-C_3N_4 nanocatalyst. Indicating that the catalytic performance of g-C_3N_4 nanocatalyst can be significantly improved by doping with the suitable metallic dopant.

The catalytic activity of the developed photocatalyst can be attributed to the various reactive species (h+, •OH, $\bullet O_2^-$, and $\bullet OH^-$) that are generated on visible light irradiation. On exposure to visible light, the electrons jump from the valence band to the conduction band, where they react with the oxygen (O_2) that is absorbed on the photocatalyst surface and produce $\bullet O_2$. The produced $\bullet O_2$ plays a vital role in the photolytic degradation of MB [23]. Ferric oxide, in its pure form, can be excited with visible light due to its large bandgap energy. However, the homogeneous structure of ferric dopped g-C_3N_4 facilitates the electron excitation and their movements in the sub-band and conduction band of ferric oxide. Thus, the holes on the VB of the dopant react with OH^-/H_2O to produce •OH. Furthermore, these holes may have a direct role in the photocatalytic degradation of MB. Ultimately, reactive oxygen species (•OH, h+, and O_2) attack MB, causing it to be oxidized. In the meantime, due to the internal electric field, the electrons present in the conduction band of the dopant may migrate and combine with holes in the valence band of graphitic carbon nitride. Thus, these electrons and holes present in the g-C_3N_4 and dopant, respectively, may result in enhanced reduction and oxidation of the developed nanocomposites [24,25]. Therefore, the prepared heterogeneous structure of the ferric doped g-C_3N_4 nanocatalyst greatly improved the photocatalytic activity. The comparative analysis for the catalytic activity of various catalysts is summarized in Table S3.

The photocatalytic stability of the catalyst is an important factor to evaluate its performance. For this, after the completion of the MB degradation, the fabric samples coated with the developed photocatalysts were removed, washed with deionized water, and used again after drying. The catalytic efficiency was evaluated 5 times and it was found that the developed photocatalysts were stable up to 5 consecutive cycles with a conversion efficiency of 99.8 %. Fig. 3 indicates that the developed samples have exceptional catalysis behavior even after 5 successive cycles. This behavior can be attributed to the structural integrity of the nanocomposites that are firmly supported on the textile substrate. This stability can be due to the enhanced aqueous stability of the developed photocatalysts. For the clarity and ease of understanding of the sample F9 digital photographs shown in Fig. 4 (i) virgin ii) g-C_3N_4/Fe coated iii) after degradation reaction iv) after washing v), recycled cotton fabric material, and (vi) MB before degradation (left) and after degradation (right). It is evident from the results that structural integrity of the sample does not change significantly even after 5 successive cycles.

3.3. FTIR

The chemical structure of the developed photocatalyst was revealed by the FTIR analysis and the results are shown in Fig. 5. The sharp bands at around 811 cm^{-1} and 1425 cm^{-1} can be attributed to the breathing modes of tri-*s*-triazine units. The absorption bands in the range of 1000 cm^{-1} to 1650 cm^{-1} can be due to typical stretching modes of the heterocyclic C–N and they arise from the extended C_3N_4 arrangement. The absorption band at 1317 cm^{-1} is attributed to the stretching vibrations of C═N. The broad spectrum in the range of 2970 cm^{-1} to 3450 cm^{-1} is due to the –NH stretch and hydroxyl (OH) functional groups, present on the surface of the photocatalysts due to the surface bonded H_2O molecules [26,27].

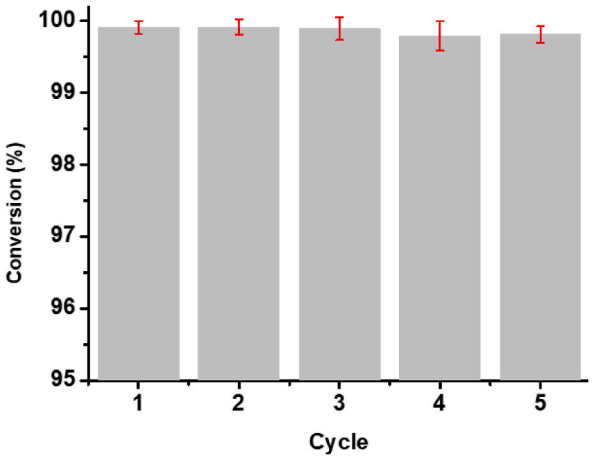

Fig. 3. Catalytic efficiency of developed nanocomposite (sample F9) after repeated use (error bars indicate the standard deviation of five (5) replicates).

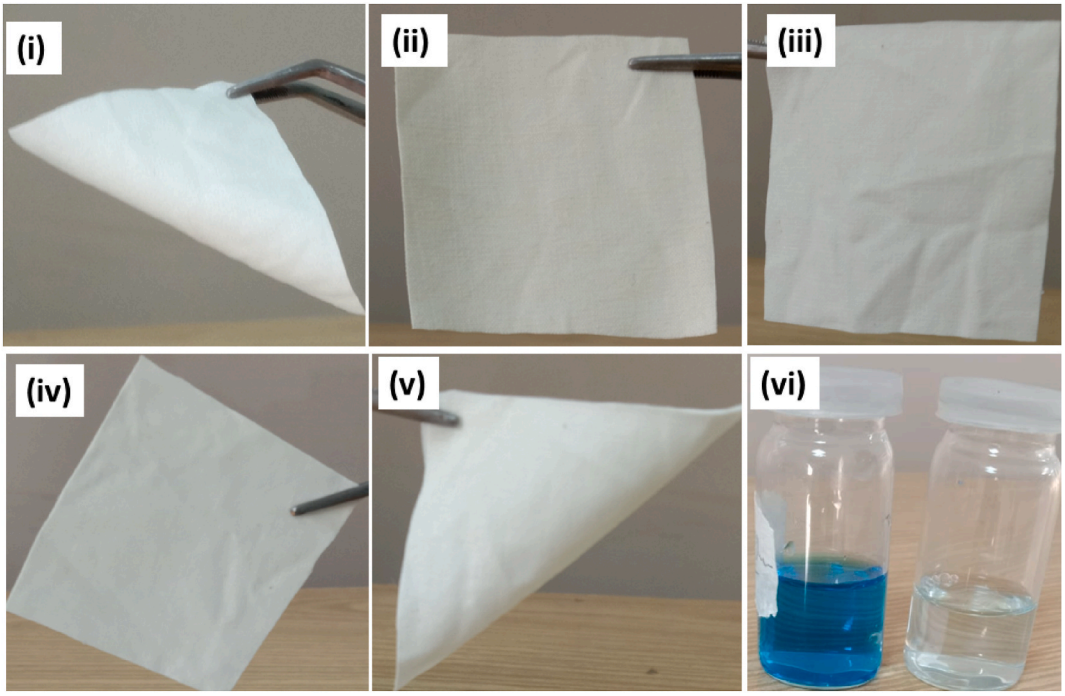

Fig. 4. Digital photographs of i) virgin ii) g-C_3N_4/Fe coated iii) after degradation reaction iv) after washing v), recycled cotton fabric (sample F9), and vi) MB before degradation (left) and after degradation (right).

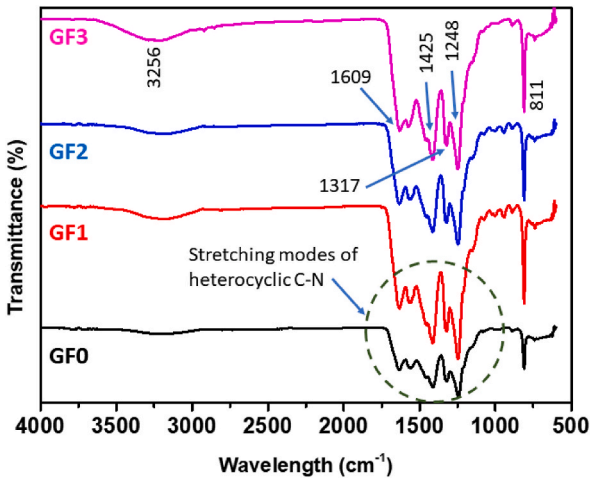

Fig. 5. FTIR spectra of various photocatalysts, developed in this study.

3.4. XRD of the nanocomposites

The crystal structure of the developed photocatalyst was determined by the XRD pattern using CuKα radiation, operated at 40 kV, 250 mA, and the results are shown in Fig. 6. It can be seen from the XRD pattern that there was a clear and strong peak around 27.1° in pure g-C_3N_4 and ferric doped nanocatalyst. It can be attributed to (002) plane due to the periodic stacking of layers of g-C_3N_4, indicating that the structural integrity of the developed nanocomposites is dominated by the g-C_3N_4 [28]. Another peak, with relatively low intensity at around 12.9°, can be attributed to the (100) plane and it arises due to the in-plane structural packing motif of g-C_3N_4 (hole-to-hole distance of nitride pores). The peaks of sample GF2, exhibited at 16.9°, 19.8°, 24.7°, 27.0°, 32.2°, 36.7°, and 41.5° are corresponding to the (111), (211), (012), (002), (220), (110), and (311) planes of ferric doped g-C_3N_4 nanocomposites [29]. It is evident that the new crystallites appear at the doping of g-C_3N_4 with ferric until the optimum doping level (Sample GF2). The addition of ferric beyond the saturation level results in the amorphous structure of the developed nanocomposites.

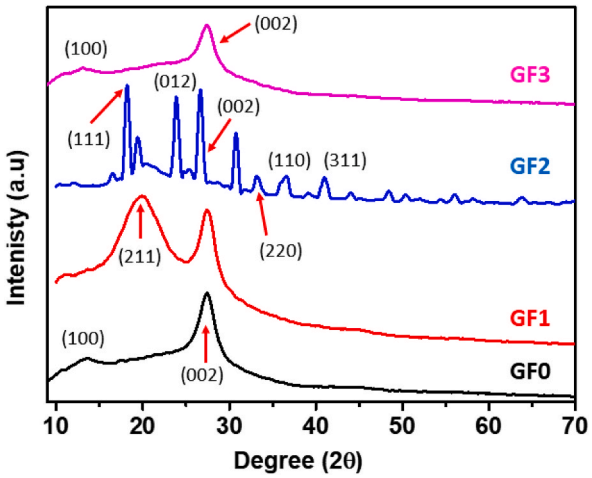

Fig. 6. XRD pattern of the synthesized nanocomposites.

3.4.1. Scanning electron microscopy (SEM)

Scanning electron microscopy was employed to observe the deposition of g-C_3N_4 and g–C_3N_4–nanosheets/α-Fe_2O_3 on the cotton fabric surface. The SEM image in Fig. 7 (a) is showing the surface of cotton fibers without coating, and (b) is showing the dense coating of g-C_3N_4 (like a paste). While the scanning electron microscopy of g–C_3N_4–nanosheets/α-Fe_2O_3 coated samples is shown in Fig. 7 (c, d, e, and f).

The image revealed the nano to micrometer scale of g–C_3N_4–nanosheets/α-Fe_2O_3 particles deposited on the fabric surface. Ferric doping is creating rough irregular clusters with rough surfaces, small agglomeration, and quasi-spherical in shape. The even distribution of the microparticles on the fabric surface was also visualized. Emphasizing the agglomeration is not followed on the larger part of the synthesized materials. Secondly, the deposition behavior was also analyzed with an increase in the concentration of ferric (0–4 ml during doping) and the number of coating cycles (1, 2, and 3). With the increase in the number of coating cycles, the deposition of g–C_3N_4–nanosheets/α-Fe_2O_3 was found more uniform and denser. Furthermore, the elemental composition of the g–C_3N_4–nanosheets/

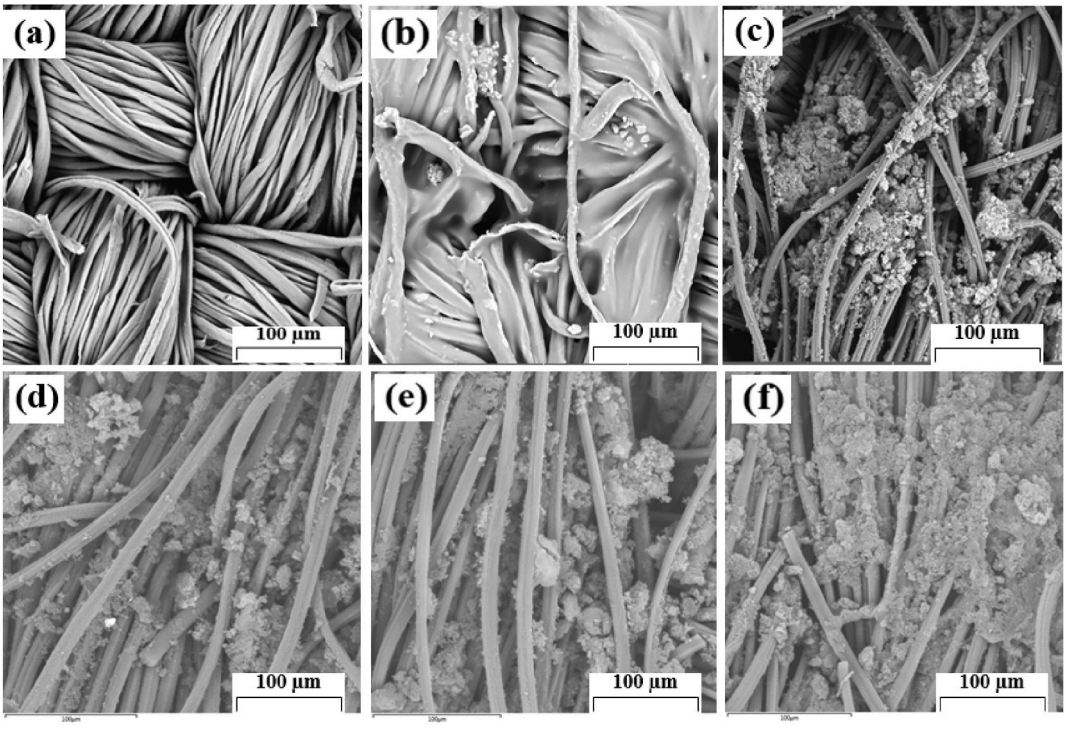

Fig. 7. SEM images for untreated cotton **(a)**, treated fabric GF0 **(b)**, treated fabric GF1 **(c)**, treated fabric GF2 **(d)**, treated fabric GF3 **(e),** and treated fabric GF4 **(f)**.

α-Fe_2O_3 coated fabric is also shown with color SEM images (Fig. S2) and an EDX Table S3. The higher contents of ferric were found with an increase in coating cycles (1, 2, and 3) for GF2 samples. The colored images of the elemental analysis, determined by the EDX are also shown in Fig. S2 (SI file). Table S4 (SI file) showed the elemental composition of g–C_3N_4–nanosheets/α-Fe_2O_3 coated fabrics determined by EDX analysis.

3.5. Antibacterial activity

ISO 20743 transfer method was followed to carry out quantitative antibacterial analysis of developed samples. The untreated cotton fabric (control) and treated fabrics (GF0, GF1, GF2, GF3, and GF4) were tested against both gram-positive (*S. aureus*) and gram-negative (*E. coli*) bacteria and obtained results have been shown in Table S5 (SI file). The results indicated that the antibacterial activity of treated samples increased with the increase in the concentration of doped material i.e., GF0 (P1, zero, concentration of $FeCl_3{\cdot}6H_2O$ (ml)) was least effective (75 %) whereas the maximum bactericidal effect (99.99 %) was observed in the case of sample GF4 (P5, concentration of $FeCl_3{\cdot}6H_2O$ (4 ml)) against *S. aureus* and *E. coli*.

It was also observed that for each set of coated fabrics, the antibacterial activity increased with increasing the number of coating layers. In the case of GF0, fabric with a single coating showed 62 % bacterial growth reduction whereas fabric with 3 coating layers was found to have a 75 % reduction in bacterial colonies.

From the results, it has been found that the fabric with a single coating layer of GF3 formulation was best suited for *S. Aureus* as it killed 99.99 % bacterial colonies (Fig. S3 (SI file)) while 99.99 % *E. Coli* bacterial reduction was observed for the fabric with 3 coating layers of the same formulation i.e., GF3. The results indicated that complete reduction (99.99) of *E. coli* occurred at a higher concentration of applied coating materials as compared to *S. Aureus*. It could be due to the fact that the cell wall of *E. coli* (gram-negative bacteria) is thicker than the cell wall of *S. Aureus* (gram-positive bacteria) which causes the attenuation of the penetration process of g-C_3N_4 into the bacterial cell membranes [30,31].

The antibacterial action of the sample GF0 (fabric coated with g-C_3N_4) is due to the graphitic carbon nitride as it has an intrinsic tendency to kill microbes. The g-C_3N_4 exhibits antibacterial action when it is exposed to visible light. Under visible light, excessive free radical species are produced in g-C3N4 which interacts with the bacterial cell membranes and ruptures it leading to apoptosis. The antibacterial activity of fabrics coated with iron-doped g-C_3N_4 was remarkably high as compared to the fabrics coated with pristine g-C_3N_4 and 99.99 % bacterial growth reduction for both gram-negative and gram-positive bacterial strains was achieved with doped g-C_3N_4. Considering the structural changes that occurred in the g-C_3N_4 after doping with $FeCl_3$, the best possible explanation for the extraordinary antibacterial action of doped g-C_3N_4 could be the presence of Fe^{+2} ions in its structure. The Fe^{+2} ions interact with essential components of bacterial cell membranes ultimately leading to cell death. The Fe^{+2} ions undergo reduction to Fe^{+} in the cytoplasm and generate reactive hydroxyl free radicals. These radicals are capable of reacting non-specifically with nucleic acid, lipids, and proteins and interrupt their structures ultimately causing bacterial cell death [32,33].

3.6. Antiviral activity

The evaluation of the antiviral efficiency of treated fabric (GF3) and untreated fabric (control) was done through a standard quantitative test method. Both control and iron-doped g-C_3N_4 loaded samples were selected. It is obvious from previous studies that metallic NPs exhibit antiviral [34,35]. The iron-doped g-C_3N_4 showed antiviral activity against different viruses types which is attributed to direct iron-doped g-C_3N_4 binding with viral enveloped glycoproteins, thus, inhibiting the penetration of viruses inside host cells, though the action mechanism is not explained well [36–39].

Cotton alone does not show any type of antiviral activity which shows that antiviral behavior associated with composites is due to composite bonded with iron-doped g-C_3N_4. The treated fabric was found to be most effective against Influenza virus and Feline Calicivirus, thus, achieving 99.45 % reduction (2.19 log10) and 99.52 % (2.30 log 10) at 2 exposure hours as compared to the control fabric as given in Table S6 (SI file). The size effect of iron-doped g-C_3N_4 composites on the antiviral activity shows interactive selectivity of Influenza Virus A with smaller particles, as reported previously for other virus types [38].

4. Conclusion

The current research reported the development of textile-based free-standing highly efficient photocatalysts containing g–C_3N_4–α-Fe_2O_3 nanocomposites by simple, versatile, sustainable, and low-cost synthesis techniques. The results revealed that the rate of MB reduction has increased with the increasing amount of developed photocatalysts and maximum degradation i.e., the optimum level was achieved in the case of sample GF2 P3. After that, the increase in the concentration of iron catalyst resulted in decreased degradation. Further, the morphology of coated fabrics was studied using SEM images, and the existence of elements was confirmed through EDX and XRD techniques. The results indicated that the antibacterial activity of treated samples increased with the increase in the concentration of doped material. The antibacterial activity of fabrics coated with iron-doped g-C_3N_4 was remarkably high as compared to the fabrics coated with pristine g-C_3N_4. Moreover, treated fabric (GF3) the iron-doped g-C_3N_4 showed antiviral activity against different viruses. Furthermore, the unique recyclability of the developed product makes it ideal for commercial applications.

Data and code availability

Data will be available on request.

Supplementary information

Added.

Ethical approval

The current study does not include human or animal subjects.

CRediT authorship contribution statement

Munir Ashraf: Conceptualization, Methodology. **Fiaz Hussain:** Formal analysis, Methodology. **Humera Aziz:** Conceptualization, Methodology. **Umair Riaz:** Formal analysis. **Muhammad Hamzah Saleem:** Formal analysis. **Amjed Javid:** Conceptualization, Formal analysis. **Anum Nosheen:** Investigation. **Azam Ali:** Investigation. **Mohammad K. Okla:** Resources, Software. **Ibrahim A. Saleh:** Resources, Software, Writing – original draft. **Ibrahim A. Alaraidh:** Resources, Software, Writing – review & editing. **Mostafa A. Abdel-Maksoud:** Resources, Software, Writing – original draft.

Declaration of competing interest

The authors declare that they have no known competing financial interests or personal relationships that could have appeared to influence the work reported in this paper.

Acknowledgment

The authors extend their appreciation to the Researchers Supporting Project Number (RSP2023R176) King Saud University, Riyadh, Saudi Arabia.

Appendix A. Supplementary data

Supplementary data to this article can be found online at https://doi.org/10.1016/j.heliyon.2023.e20822.

References

[1] C. Chen, G. Reniers, Risk assessment of processes and products in industrial biotechnology, Sustainability and Life Cycle Assessment in Industrial Biotechnology 173 (2020) 255–279, https://doi.org/10.1007/10_2018_74.
[2] W.Y. Wang, J.C. Chiou, J. Yip, K.F. Yung, C.W. Kan, Development of durable antibacterial textile fabrics for potential application in healthcare environment, Coatings 10 (2020) 520, https://doi.org/10.3390/coatings10060520.
[3] A. Kramer, I. Schwebke, G. Kampf, How long do nosocomial pathogens persist on inanimate surfaces? A systematic review, BMC Infect. Dis. 6 (2006) 1–8, https://doi.org/10.1186/1471-2334-6-130.
[4] Q. Cao, J.S. Barrio, M. Antonietti, B. Kumru, M. Shalom, B.V. Schmidt, Photoactive graphitic carbon nitride-based gel beads as recyclable photocatalysts, ACS Appl. Polym. Mater. 2 (2020) 3346–3354, https://doi.org/10.1021/acsapm.0c00453.
[5] D. Bhatia, N.R. Sharma, J. Singh, R.S. Kanwar, Biological methods for textile dye removal from wastewater: A review, Critical Reviews In Environmental Science and Technology 47 (2017) 1836–1876, https://doi.org/10.1080/10643389.2017.1393263.
[6] P. Bhatt, S.C. Pandey, S. Joshi, P. Chaudhary, V.M. Pathak, Y. Huang, X. Wu, Z. Zhou, S. Chen, Nanobioremediation: A sustainable approach for the removal of toxic pollutants from the environment, J Hazard Mater 427 (2022), 128033, https://doi.org/10.1016/j.jhazmat.2021.128033.
[7] K. Song, M. Mohseni, F. Taghipour, Application of ultraviolet light-emitting diodes (UV-LEDs) for water disinfection: A review, Water Res 94 (2016) 341–349, https://doi.org/10.1016/j.watres.2016.03.003.
[8] D. Rodriguez-Padron, A.R. Puente-Santiago, A.M. Balu, M.J. Muñoz-Batista, R. Luque, Environmental catalysis: present and future, ChemCatChem 11 (2019) 18–38, https://doi.org/10.1002/cctc.201801248.
[9] P. Karthik, R. Vinoth, P. Selvam, E. Balaraman, M. Navaneethan, Y. Hayakawa, B. Neppolian, A visible-light active catechol–metal oxide carbonaceous polymeric material for enhanced photocatalytic activity, Journal of Materials Chemistry A 5 (2017) 384–396, https://doi.org/10.1039/C6TA07685H.
[10] H. Chakhtouna, H. Benzeid, N. Zari, A.e.k. Qaiss, R. Bouhfid, Recent progress on Ag/TiO 2 photocatalysts: Photocatalytic and bactericidal behaviors, Environ Sci Pollut Res Int 28 (2021) 44638–44666, https://doi.org/10.1007/s11356-021-14996-y.
[11] G. Yang, Z. Yan, T. Xiao, Preparation and characterization of SnO2/ZnO/TiO2 composite semiconductor with enhanced photocatalytic activity, Applied Surface Science 258 (2012) 8704–8712, https://doi.org/10.1016/j.apsusc.2012.05.078.
[12] Q. Zheng, H. Shen, D. Shuai, Emerging investigators series: advances and challenges of graphitic carbon nitride as a visible-light-responsive photocatalyst for sustainable water purification, Environmental Science: Water Research & Technology 3 (2017) 982–1001, https://doi.org/10.1039/C7EW00159B.
[13] N. Rono, J.K. Kibet, B.S. Martincigh, V.O. Nyamori, A review of the current status of graphitic carbon nitride, Critical Reviews in Solid State and Materials Sciences 46 (2021) 189–217, https://doi.org/10.1080/10408436.2019.1709414.
[14] S. Kamath, H. Manohara, D. Mondal, S.K. Nataraj, Nanocomposite-based high-performance adsorptive water filters: Recent advances, limitations, nanotoxicity and their environmental implications, Environmental Science. Nano 7 (2022), https://doi.org/10.1039/D2EN00155A.
[15] M. Majdoub, Z. Anfar, A. Amedlous, Emerging chemical functionalization of g-C3N4: covalent/noncovalent modifications and applications, ACS Nano 14 (2020) 12390–12469, https://doi.org/10.1021/acsnano.0c06116.
[16] G. Liao, F. He, Q. Li, L. Zhong, R. Zhao, H. Che, H. Gao, B. Fang, Emerging graphitic carbon nitride-based materials for biomedical applications, Progress in Materials Science 112 (2020), 100666, https://doi.org/10.1016/j.pmatsci.2020.100666.
[17] S. Vinoth, K.S. Devi, A. Pandikumar, A Comprehensive Review on Graphitic Carbon Nitride Based Electrochemical and Biosensors for Environmental and Healthcare Applications, in: TrAC Trends in Analytical Chemistry, vol. 140, 2021, 116274, https://doi.org/10.1016/j.pmatsci.2020.100666.

[18] J. Xu, Z. Wang, Y. Zhu, Enhanced visible-light-driven photocatalytic disinfection performance and organic pollutant degradation activity of porous g-C3N4 nanosheets, ACS Appl Mater Interfaces 9 (2017) 27727–27735, https://doi.org/10.1021/acsami.7b07657.
[19] H. Sun, Y. Cao, L. Feng, Y. Chen, Immobilizing photogenerated electrons from graphitic carbon nitride for an improved visible-light photocatalytic activity, Sci Rep 6 (2016) 1–10, https://doi.org/10.1038/srep22808.
[20] P.H. Linh, P. Do Chung, N. Van Khien, V.T. Thu, T.N. Bach, L.T. Hang, N.M. Hung, V.D. Lam, A Simple Approach for Controlling the Morphology of G-C3n4 Nanosheets with Enhanced Photocatalytic Properties, Diamond and Related Materials vol. 111 (2021), 108214, https://doi.org/10.1016/j.diamond.2020.108214.
[21] A. Hayat, A.G. Al-Sehemi, K.S. El-Nasser, T. Taha, A.A. Al-Ghamdi, J.A.S. Syed, M.A. Amin, T. Ali, T. Bashir, A. Palamanit, Graphitic carbon nitride (g–C3N4)–based semiconductor as a beneficial candidate in photocatalysis diversity, International Journal of Hydrogen Energy 47 (2022) 5142–5191, https://doi.org/10.1016/j.ijhydene.2021.11.133.
[22] F. Hussain, S.M. Shaban, J. Kim, D.H. Kim, One-pot synthesis of highly stable and concentrated silver nanoparticles with enhanced catalytic activity, Korean Journal of Chemical Engineering 36 (2019) 988–995, https://doi.org/10.1007/s11814-019-0270-6.
[23] M. Danish, M.S. Athar, I. Ahmad, M.Z. Warshagha, Z. Rasool, M. Muneer, Highly efficient and stable Fe2O3/g-C3N4/GO nanocomposite with Z-scheme electron transfer pathway: Role of photocatalytic activity and adsorption isotherm of organic pollutants in wastewater, Applied Surface Science 604 (2022), 154604, https://doi.org/10.1016/j.apsusc.2022.154604.
[24] S. Tonda, S. Kumar, S. Kandula, V. Shanker, Fe-doped and-mediated graphitic carbon nitride nanosheets for enhanced photocatalytic performance under natural sunlight, Journal of Materials Chemistry A 2 (2014) 6772–6780, https://doi.org/10.1039/C3TA15358D.
[25] V. Hasija, P. Raizada, V.K. Thakur, T. Ahamad, S.M. Alshehri, S. Thakur, V.H. Nguyen, Q. Van Le, P. Singh, An overview on photocatalytic sulfate radical formation via doped graphitic carbon nitride for water remediation, Current Opinion in Chemical Engineering 37 (2022), 100841, https://doi.org/10.1016/j.coche.2022.100841.
[26] H. Wang, W. He, H. Wang, F. Dong, In situ FT-IR investigation on the reaction mechanism of visible light photocatalytic NO oxidation with defective g-C3N4, Science Bulletin 63 (2018) 117–125, https://doi.org/10.1016/j.scib.2017.12.013.
[27] T. Guo, K. Wang, G. Zhang, X. Wu, A novel α-Fe2O3@ g-C3N4 catalyst: synthesis derived from Fe-based MOF and its superior photo-Fenton performance, Applied Surface Science 469 (2019) 331–339, https://doi.org/10.1016/j.apsusc.2018.10.183.
[28] F. Chang, Y. Xie, C. Li, J. Chen, J. Luo, X. Hu, J. Shen, A facile modification of g-C3N4 with enhanced photocatalytic activity for degradation of methylene blue, Applied Surface Science 280 (2013) 967–974, https://doi.org/10.1016/j.apsusc.2013.05.127.
[29] M.A. Karimi, M. Iliyat, M. Atashkadi, M. Ranjbar, A. Habibi-Yangjeh, Microwave-assisted synthesis of the Fe2O3/g-C3N4 nanocomposites with enhanced photocatalytic activity for degradation of methylene blue, Journal- Chinese Chemical Society Taipei 67 (2020) 2032–2041, https://doi.org/10.1002/jccs.202000068.
[30] A. Nosheen, M.T. Hussain, M. Khalid, A. Javid, H. Aziz, S. Iqbal, M. Ashraf, S. Ali, Development of Protective Cotton Textiles Against Biohazards and Harmful UV Radiation Using Eco-Friendly Novel Fiber-Reactive Bioactive Agent, Process Safety and Environmental Protection 165 (2022), https://doi.org/10.1016/j.psep.2022.07.035.
[31] S. Akram, A. Javid, M. Ashraf, Silver electroless plating on aminated graphene oxide-based cotton fabric for electromagnetic interference shielding and bioactivity, Materials Science and Engineering: B 288 (2023), 116159, https://doi.org/10.1016/j.mseb.2022.116159.
[32] A. Nosheen, M.T. Hussain, M. Ashraf, K. Iqbal, A novel approach to modify and functionalize acid black 1 dye for antimicrobial and UV protective textiles, Dyes and Pigments 205 (2022), 110486, https://doi.org/10.1016/j.dyepig.2022.110486.
[33] A. Nosheen, M. Khalid, S. Manzoor, M. Ashraf, Z. Xue, S. Akram, D.S. Khan, S. Urooj, A.H. Hashmi, Pilot-scale production of highly durable bioactive and UV-protective cotton fabric by electroless deposition of copper oxide on cotton fabric 4 (2022) 1–23, https://doi.org/10.1007/s10570-022-05009-3.
[34] F. Pilaquinga, J. Morey, M. Torres, R. Seqqat, M.d.l.N. Pina, Silver nanoparticles as a potential treatment against SARS-CoV-2: A review, Wiley Interdiscip Rev Nanomed Nanobiotechnol 13 (2021), e1707, https://doi.org/10.1002/wnan.1707.
[35] D.X. Xiang, Q. Chen, L. Pang, C.l. Zheng, Inhibitory effects of silver nanoparticles on H1N1 influenza A virus in vitro, J Virol Methods 178 (2011) 137–142, https://doi.org/10.1016/j.jviromet.2011.09.003.
[36] J.L. Elechiguerra, J.L. Burt, J.R. Morones, A.C. Bragado, X. Gao, H.H. Lara, M.J. Yacaman, Interaction of silver nanoparticles with HIV-1, J Nanobiotechnology 3 (2005) 1–10, https://doi.org/10.1186/1477-3155-3-6.
[37] L. Lu, R.W.Y. Sun, R. Chen, C.K. Hui, C.M. Ho, J.M. Luk, G.K. Lau, C.M. Che, Silver nanoparticles inhibit hepatitis B virus replication, Antivir Ther 13 (2008) 253–262, https://doi.org/10.1177/135965350801300210.
[38] H. Lara, E.N. Garza-Trevin, L. Turrent, D.K. Singh, Silver nanoparticles are broad-spectrum bactericidal and virucidal compounds, J Nanobiotechnology 9 (2011) 30, https://doi.org/10.1186/1477-3155-9-30.
[39] A. Ali, F. Hussain, S. Attacha, A. Kalsoom, W.A. Qureshi, M. Shakeel, J. Militky, B. Tomkova, D. Kremenakova, Development of Novel Antimicrobial and Antiviral Green Synthesized Silver Nanocomposites for the Visual Detection of Fe3+ Ions, Nanomaterials (Basel) 11 (2021) 2076–2094, https://doi.org/10.3390/nano11082076.